

# A multi-term solution of the space-time Boltzmann equation for electrons in gaseous and liquid argon

G. J. Boyle,<sup>1</sup> W. J. Tattersall,<sup>1,2</sup> D. G. Cocks,<sup>1</sup> R. P. McEachran,<sup>2</sup> and R. D. White<sup>1</sup>

<sup>1</sup>*College of Science, Technology & Engineering,  
James Cook University, Townsville, QLD 4810, Australia*

<sup>2</sup>*Research School of Physical Sciences and Engineering,  
Australian National University, Canberra, ACT 0200, Australia*

## Abstract

In a recent paper [1] the scattering and transport of excess electrons in liquid argon in the hydrodynamic regime was investigated, generalizing the seminal works of Lekner and Cohen [2, 3] with modern scattering theory techniques and kinetic theory. In this paper, the discussion is extended to the non-hydrodynamic regime through the development of a full multi-term space-time solution of Boltzmann's equation for electron transport in gases and liquids using a novel operator-splitting method. A Green's function formalism is considered that enables flexible adaptation to various experimental systems. The spatio-temporal evolution of electrons in liquids in the hydrodynamic regime is studied for a benchmark model Percus-Yevick liquid as well as for liquid argon. The temporal evolution of Franck-Hertz oscillations are observed for liquids, with striking differences in the spatio-temporal development of the velocity distribution function components between the uncorrelated gas and true liquid approximations in argon. Transport properties calculated from the non-hydrodynamic theory in the long time limit, and under steady-state Townsend conditions, are benchmarked against hydrodynamic transport coefficients.

## I. INTRODUCTION

The study of electron transport in dense gases and liquids is of interest in understanding the fundamental microscopic scattering processes involved, and to technological applications including liquid-state electronics [4], high-energy particle detectors [5–8], plasma medicine [9–12] and radiation dosimetry [13–16]. For these technologies to reach their full potential requires a detailed understanding of the full spatio-temporal behaviour of electrons in dense gases, liquids, and other bio-structures, typically under non-equilibrium conditions.

In a recent paper [1] the transport of excess electrons in liquid argon was considered from ab initio liquid phase cross-sections calculated using the Dirac-Fock scattering equations. The approach detailed in the seminal works by Lekner and Cohen [2, 3] has been revisited with modern scattering theory techniques, where the original treatment was extended to consider multipole polarizabilities and a non-local treatment of exchange. With an increase in density, several important density effects become significant, most notably (i) the coherent scattering from multiple scattering centres, (ii) the screening of the long range polarization potential due to induced multipoles in the bulk, and (iii) the contribution of the bulk to the effective potential experienced by the electron. Transport coefficients such as drift velocities and characteristic energies calculated in the hydrodynamic regime with our hydrodynamic multi-term Boltzmann equation solution were in good agreement with swarm experiment measurements in both gas- and liquid-phase argon [17]. In this work we extend the discussion to an investigation of liquid state in the non-hydrodynamic regime, using the same electron-argon potentials and cross-sections presented in [1].

The solution of the the full temporal-, spatial- and energy-dependent Boltzmann equation is formidable, both mathematically and computationally. Historically, the majority of kinetic theory investigations have focused on the hydrodynamic regime where spatial gradients are small, and have considered increasingly complex space- and time-dependent hydrodynamic behaviours and field configurations (see reviews [18–22]). In situations where the hydrodynamic regime is not applicable, the space-time dependence of the phase space distribution function cannot be projected onto the number density and a density gradient expansion is no longer valid. Instead the configuration-space dependence of the Boltzmann equation must be treated on equal footing with the energy-space dependence, which makes for a difficult problem even for simple geometries [23–25]. It is no surprise that systematic studies

of non-hydrodynamic phenomena lag behind their hydrodynamic counterparts. The prototypical example of non-hydrodynamic phenomena is the Frank-Hertz experiment [26, 27], which helped lay the foundations for quantum and atomic physics. Extensive theoretical studies of non-hydrodynamic electron phenomena have been performed including field free spatial relaxation [28], and spatial relaxation in the presence of uniform [29–32], non-uniform [33] and periodic electric fields [34–36]. Similar kinetic studies on the spatial relaxation of electrons in uniform and spatially periodic fields have been performed by Golubovskii et al. [37–40]. Li and co-workers have considered arbitrary electric and magnetic field configurations with a multi-term analysis [19, 41, 42]. Solution of the Boltzmann equation for electrons including both the space and time dependence have also recently been performed [43–45], however these authors restricted their calculations to a two-term approximation in Legendre polynomials in order to make the problem computationally feasible. Limitations of the two-term approximation for molecular gases are well known [46]. Prior to [1], all studies of electron transport in liquids were in the hydrodynamic or spatially homogeneous regimes, and restricted to the two-term approximation.

In this study, we present a full multi-term space-time dependent solution of Boltzmann’s equation, capable of handling highly non-equilibrium electron transport in dilute gases, dense gases and liquids under non-hydrodynamic conditions. To our knowledge, this is the first time such a complete solution of Boltzmann’s equation has been developed. In addition, by solving for the spatio-temporal evolution of the Boltzmann equation Green’s function, the technique is quite general in its application, enabling various experimental configurations (temporal and spatial initial and boundary conditions) and practical devices to be modelled from a single solution. This work extends the Boltzmann equation framework to applications and accuracies comparable to those achieved using the Monte-Carlo simulations of Petrovic, Dujko and co-workers [47–49].

We begin the paper in Section II with a brief overview of the multi-term solution of Boltzmann’s equation for electrons in structured materials, such as liquids. We then detail our operator splitting treatment of the space, time and energy dependence in Section III. In Section IV we present solutions for a model hard-sphere liquid system with a Percus-Yevick structure factor used to simulate a prototypical liquid with realistic pair correlations. A simple inelastic channel is included to induce periodic oscillatory structures (an idealized version of the well known Frank-Hertz experiment [27]) which can act as a non-hydrodynamic

benchmark. Lastly, in Section V we investigate the temporal and spatial evolution of the phase-space distribution for electrons in liquid argon, using microscopic cross-sections which have been derived previously [1]. The issues with treating liquid systems as gaseous systems with increased density, and the implications for various applications including liquid argon time projection chambers, are highlighted.

## II. THEORY

The fundamental kinetic equation describing the evolution of an electron swarm in a gaseous or liquid background medium subject to an electric field,  $\mathbf{E}$ , is the Boltzmann equation for the phase-space distribution function  $f \equiv f(\mathbf{r}, \mathbf{v}, t)$  [50]:

$$\left( \frac{\partial}{\partial t} + \mathbf{v} \cdot \frac{\partial}{\partial \mathbf{r}} + \frac{e\mathbf{E}}{m} \cdot \frac{\partial}{\partial \mathbf{v}} \right) f = -J(f), \quad (1)$$

where  $t$  is time, and  $\mathbf{r}$ ,  $\mathbf{v}$ ,  $e$  and  $m$  are the position, velocity, charge and mass of the electron respectively. The collision operator  $J(f)$  accounts for interactions between the electrons and the background material, and describes the effect of collisions on the distribution function at a fixed position and velocity. In essence the Boltzmann equation represents an extension of the continuity equation to phase-space. A solution of equation (1) for the distribution function yields all relevant information about the system. Macroscopic transport properties including mean energy and drift velocity can then be found via averages over the ensemble, as detailed in Section III F.

The starting point for most modern solutions of the Boltzmann equation is the decomposition of the angular part of the velocity dependence of equation (1) in terms of spherical harmonics [50]. If there is a single preferred direction in the system, e.g. due to an electric field in plane parallel geometry, then the angular dependence of the velocity component can be adequately described by a simpler expansion in terms of Legendre polynomials. For the plane-parallel geometry considered in this work,  $f(\mathbf{v}, \mathbf{r}, t) \rightarrow f(v, z, \mu, t)$ , where  $\mu = \hat{\mathbf{v}} \cdot \hat{\mathbf{E}} = \cos \chi$ , such that

$$f(\mathbf{v}, \mathbf{r}, t) = \sum_{l=0}^{\infty} f_l(v, z, t) P_l(\mu), \quad (2)$$

where  $P_l$  is the  $l$ -th Legendre polynomial. Upon substituting the expansion (2) into equation (1) and equating the coefficients of the Legendre polynomials results in the following system of coupled partial differential equations for the  $f_l$ :

$$\frac{\partial f_l}{\partial t} + \sum_{p=\pm 1} \Delta_l^{(p)} \left(\frac{2}{m}\right)^{\frac{1}{2}} \left[ U^{1/2} \frac{\partial}{\partial z} + eE \left( U^{\frac{1}{2}} \frac{\partial}{\partial U} + p \frac{(l + \frac{3p+1}{2})}{2} U^{-\frac{1}{2}} \right) \right] f_{l+p} = -J_l(f_l), \quad (3)$$

for  $l = 0, 1, 2, \dots, \infty$ , where  $U = \frac{1}{2}mv^2$ ,  $J_l$  is the Legendre decomposition of the collision operator, and

$$\Delta_l^{(+1)} = \frac{l}{(2l-1)}; \quad \Delta_l^{(-1)} = \frac{(l+1)}{(2l+3)}. \quad (4)$$

Equation (3) represents an infinite set of coupled partial differential equations for the expansion coefficients,  $f_l$ . In practice, one must truncate the series (2) at a sufficiently high index,  $l = l_{\max}$ . The history of charged particle transport in gases and liquids has been dominated by the ‘two-term approximation’, i.e., where only the first two terms have been included. The assumption of quasi-isotropy necessary for the two-term approximation is violated in many situations, particularly when inelastic collisions are included [51] or when higher order moments are probed [1]. Such an assumption is not necessary in our multi-term formalism. Instead, the truncation parameter  $l_{\max}$  is treated as a free parameter that is incremented until some convergence criterion is met on the distribution function or its velocity moments.

In order to solve equation (3) we require the collision operators for all of the relevant collisional processes, and their representations in terms of Legendre polynomials,  $J_l$ . If we assume that the neutral background material is at rest and in thermal equilibrium at a temperature  $T_0$ , then the collision operator is linear in the swarm approximation. Below we detail the specific forms of the collision operator for particle-conserving elastic and inelastic collisions employed. A further expansion of each collision integral with respect to the ratio of swarm particle mass to neutral particle mass,  $m/m_0$ , has been performed. Because this ratio is small for electrons in argon, only the leading term of this expansion was taken into account for each collision process and in each equation of the system (3). The total collision operator can be separated for each of the different types of processes, e.g.

$$J_l = J_l^{\text{el}} + J_l^{\text{exc}}, \quad (5)$$

where  $J_l^{\text{el}}$  and  $J_l^{\text{exc}}$  are the elastic and inelastic collision operators, respectively. For dense mediums and low electron energies, the de Broglie wavelength of the electron is comparable to the average inter-particle spacing  $\sim n_0^{-1/3}$ . The electron wave is then scattered coherently from multiple scattering centres in the medium. Cohen and Lekner [3] showed how to account for coherent scattering using a two-term approximation, which has since been extended to a multi-term regime [50, 52]. The Legendre projections of the elastic collision operator in the small mass ratio limit were shown to be:

$$J_l^{\text{el}}(f_l) = \begin{cases} -\frac{2m}{m_0}U^{-\frac{1}{2}}\frac{\partial}{\partial U}\left[U^{\frac{3}{2}}\nu_1^{\text{el}}(U)\left(f_0 + k_b T_0 \frac{\partial f_0}{\partial U}\right)\right] & l = 0, \\ \tilde{\nu}_l^{\text{el}}(U)f_l(U) & l \geq 1. \end{cases} \quad (6)$$

Here,  $m_0$  is the mass of the background neutral,  $k_b$  is Boltzmann's constant, and

$$\nu_l^{\text{el}}(U) = n_0 \left(\frac{2U}{m}\right)^{\frac{1}{2}} \left(2\pi \int_0^\pi \sigma(U, \chi) [1 - P_l(\cos \chi)] \sin \chi d\chi\right), \quad (7)$$

are the usual binary collision frequencies. A collision frequency,  $\nu$ , is related to the corresponding cross section,  $\sigma$ , via  $\nu = n_0 \left(\frac{2U}{m}\right)^{\frac{1}{2}} \sigma(U)$ . The  $\tilde{\nu}_l^{\text{el}}(v)$  in equation (6) are the structure-modified counterparts to  $\nu_l^{\text{el}}(U)$ , i.e.,

$$\tilde{\nu}_l^{\text{el}}(U) = n_0 \left(\frac{2U}{m}\right)^{\frac{1}{2}} \left(2\pi \int_0^\pi \Sigma(U, \chi) [1 - P_l(\cos \chi)] \sin \chi d\chi\right), \quad (8)$$

where  $\Sigma(U, \chi)$  is the effective differential cross-section

$$\Sigma(U, \chi) = \sigma(U, \chi) S \left(\frac{2}{\hbar} \sqrt{2mU} \sin \frac{\chi}{2}\right), \quad (9)$$

which then accounts for coherent scattering effects through the static structure factor,  $S$  [3]. At higher energies, the de Broglie wavelength becomes much less than the inter-particle spacing and the effects of coherent scattering are no longer important. In this limit, the binary scattering approximation is recovered, i.e.,  $\Sigma \rightarrow \sigma$  and  $\tilde{\nu}_l^{\text{el}} \rightarrow \nu_l^{\text{el}}$ .  $\nu_1^{\text{el}}$  is more commonly known as the momentum transfer collision frequency,  $\nu_m$ , which is associated with the momentum transfer cross section,  $\sigma_m$ . Similarly,  $\tilde{\nu}_m = \tilde{\nu}_1^{\text{el}}$  is known as the effective momentum transfer collision frequency. We will adopt this convention in the following discussions.

At higher fields, incoherent inelastic scattering effects, such as electronic excitations, need to be considered [50, 52]. By considering only a single inelastic channel, and assuming neutral particles are in the ground state, the excitation collision operator is

$$J_l^{\text{exc}}(f_l) = \nu^{\text{exc}}(U) f_l(U) - \begin{cases} \left(\frac{U+U_I}{U}\right)^{\frac{1}{2}} \nu^{\text{exc}}(U+U_I) f_l(U+U_I), & l=0, \\ 0, & l \geq 1. \end{cases} \quad (10)$$

where  $U_I$  is the threshold energy associated with the excitation collision frequency  $\nu^{\text{exc}}$ .

### III. SOLUTION TECHNIQUE

Boltzmann's equation is a non-linear integro-differential equation involving three spatial dimensions, three velocity dimensions and time. The Boltzmann equation consists of two parts; an advective component (in phase space) and a component representing collisions. It is a formidable task to solve the Boltzmann equation numerically, using a single numerical scheme for both components and a single time-stepping method. Because of the complexity, we choose to replace the task of solving the full Boltzmann equation by the task of solving the configuration-space transport, the energy-space transport and the contributions due to collisions separately, then combining the results in a manner that appropriately approximates the full solution. This can be achieved via the technique known as operator splitting [53].

To this end, the Legendre polynomial expansion of Boltzmann's equation in plane parallel geometry given in equation (3) can be represented as

$$\frac{\partial f_l}{\partial t} + S_Z(f_l) + S_U(f_l) = 0, \quad (11)$$

where

$$S_Z(f_l) = \sum_{p=\pm 1} \Delta_l^{(p)} \left(\frac{2}{m}\right)^{1/2} U^{1/2} \frac{\partial}{\partial z} f_{l+p}, \quad (12)$$

$$S_U(f_l) = \sum_{p=\pm 1} \Delta_l^{(p)} \left(\frac{2}{m}\right)^{1/2} eE \left( U^{1/2} \frac{\partial}{\partial U} + p \frac{\left(l + \frac{3p+1}{2}\right)}{2} U^{-1/2} \right) f_{l+p} + J_l(f_l). \quad (13)$$

#### A. Operator splitting

The simplest method of operator splitting, and the method employed in this paper, is Lie-Trotter splitting [54, 55], which employs two separate operators, e.g.  $S_Z$  and  $S_U$ , in a sequential order. If

$$\frac{\partial f}{\partial t} + S_Z(f) + S_U(f) = 0, \quad (14)$$

then the Lie-Trotter algorithm is

$$\frac{\partial f^*}{\partial t} + S_Z(f^*) = 0, \text{ with } t \in [t^n, t^{n+1}] \text{ and } f^*(t^n) = f(t^n), \quad (15)$$

$$\frac{\partial f^\#}{\partial t} + S_U(f^\#) = 0, \text{ with } t \in [t^n, t^{n+1}] \text{ and } f^\#(t^n) = f^*(t^{n+1}), \quad (16)$$

so that  $f(t^{n+1}) = f^\#(t^{n+1})$ , where  $t^n$  and  $t^{n+1}$  are successive times. This simple method can be shown to be only accurate to first order in time, and there are many other methods available that offer higher order accuracy and often include additional advantageous properties [55–61]. The major reason for this particular choice of operator splitting algorithm is that if  $S_Z$  is treated in an explicit manner, and  $S_U$  is treated in an implicit manner, then the result is essentially the Douglas class of the Alternating Direction Implicit schemes [62, 63], which is particularly successful at accurately capturing the steady-state solution. Accurately and consistently determining the steady-state solution can be a problem for general operator splitting methods [64].

The isolation of the configuration-space dependence to the operator  $S_Z$  makes this particular scheme an example of dimensional splitting. We can now investigate how we treat the configuration-space advection and energy-space advection and collision components numerically in detail.

## B. Configuration-space advection

The operator involving the configuration-space dependence,  $S_z$ , is given by equation (12), which represents a coupled homogeneous advection equation. As there are no derivatives of  $U$  present in  $S_z$ , the configuration-space dependence can be solved independently for different values of  $U$  which is huge simplification when a discretization in energy space is used. The coupled advection equation can be simplified as follows:

$$\frac{\partial}{\partial t} f_l + U^{\frac{1}{2}} \Delta_l^{(-)} \frac{\partial}{\partial z} f_{l-1} + U^{\frac{1}{2}} \Delta_l^{(+)} \frac{\partial}{\partial z} f_{l+1} = 0, \quad (17)$$

which can be written in matrix form,

$$\frac{\partial}{\partial t} \mathbf{f} + \mathbf{A} \frac{\partial}{\partial z} \mathbf{f} = \mathbf{0} \quad (18)$$



where  $\mathbf{f} = [f_0, f_1, \dots, f_{l_{max}}]$  and

$$\mathbf{A} = U^{\frac{1}{2}} \begin{bmatrix} 0 & \Delta_0^{(+)} & & & \\ \Delta_1^{(-)} & 0 & \Delta_1^{(+)} & & \\ & \ddots & \ddots & \ddots & \\ & & \Delta_{l_{max}-1}^{(+)} & 0 & \Delta_{l_{max}-1}^{(+)} \\ & & & \Delta_{l_{max}}^{(-)} & 0 \end{bmatrix}. \quad (19)$$

By letting  $\mathbf{A} = \mathbf{R}\mathbf{\Lambda}\mathbf{R}^{-1}$ , where  $\mathbf{\Lambda}$  is a matrix of eigenvalues of  $\mathbf{A}$  on the diagonal, and  $\mathbf{R}$  are the associated eigenvectors, then

$$\frac{\partial}{\partial t} \mathbf{g} + \mathbf{\Lambda} \frac{\partial}{\partial z} \mathbf{g} = \mathbf{0}, \quad (20)$$

where  $\mathbf{g} = \mathbf{R}^{-1}\mathbf{f}$ , which now represents a set of uncoupled, homogeneous advection equations. It follows from the method of characteristics [65], that

$$\mathbf{g}(t, z) = \mathbf{g}(0, z - \mathbf{\Lambda}t). \quad (21)$$

Even in this extremely simple form, the solution can be troublesome. When discretized, the set of values  $z - \mathbf{\Lambda}t$  are unlikely to align with existing  $z$  values, and hence some form of interpolation is required. It can be shown that linear interpolation is equivalent to a first order upwind finite volume method scheme [66]. First order methods have the advantage of being well behaved and can be used to conserve mass etc. with no unwanted, unphysical oscillations, but have the disadvantage of introducing extra numerical diffusion, particularly around regions of sharp variation [67]. Higher order methods perform better at controlling unwanted diffusion but can lead to problematic, oscillatory and unphysical solutions. Rather than straightforward interpolation, we choose to employ a variation of a technique well known in fluid transport, the SHASTA algorithm of Boris and Book [68]. The SHASTA algorithm approach, termed flux-corrected transport (FCT), leads to a class of Eulerian finite-difference algorithms which strictly enforce the non-negative property of realistic mass and energy densities. As a result, steep gradients and shocks can be handled particularly well, which is a useful property when modelling transport under non-hydrodynamic conditions. A FCT algorithm consists conceptually of two major stages, a transport or convective stage, followed by an anti-diffusive or corrective stage.

We employ a simplified version of the full FCT algorithm to numerically approximate  $\mathbf{g}(0, z - \mathbf{\Lambda}t)$ . Let us consider the evolution of  $\mathbf{g}(t, z)$  for a single  $\mathbf{\Lambda}$ , i.e.,  $g(t, z; \Lambda)$ , over a time

interval of  $\Delta t$ , with a uniform configuration-space mesh with spacing  $\Delta z$ . By discretizing in this way,  $z_j = j\Delta z$  for  $j = 1, 2, \dots, n_z - 1$ , and  $t_{n+1} = t_n + \Delta t$ . The algorithm is as follows:

**1. Shift:** The elements of  $g(t, z; \Lambda)$  are shifted to the node closest to  $z - \beta$ , where  $\beta = \frac{\Delta t}{\Delta z} \Lambda$ .

This may result in an ‘overshoot’, but we can then propagate the shifted solution (in step 2) either forwards or backwards in time as appropriate. The purpose of this step is to overcome time step limitations due to the Courant-Friedrichs-Levy (CFL) condition [69], which allows us to choose arbitrary time step sizes with respect to the configuration-space convergence (sufficiently small time steps are still necessary for the operator splitting accuracy etc.). By shifting to the nearest node, the CFL condition

$$|\beta| = \frac{\Delta t}{\Delta z} |\Lambda| \leq 1 \quad (22)$$

for the remaining advection is always satisfied.

**2. Advection with additional diffusion:** The advection algorithm employed is given by

$$g_j^{n+1} = g_j^n - \frac{\beta'}{2} (g_{j+1}^n - g_{j-1}^n) + \left( \gamma + \frac{\beta'^2}{2} \right) (g_{j+1}^n - 2g_j^n + g_{j-1}^n), \quad (23)$$

where  $g_j^{n+1} = g(t_{n+1}, z_j)$ , and

$$\gamma = \left[ 0, \frac{\beta'}{2} \right], \quad (24)$$

is the additional numerical diffusion. The dimensionless advancement  $\beta' = \beta - \lfloor \beta \rfloor$  accounts for the shift that has been applied in step 1. Note that  $\beta'$  may be opposite in sign to  $\beta$ , which corresponds to an overshoot in step 1. However, this does not adversely affect the procedure. If  $\gamma = 0$ , then equation (23) is the well known Lax-Wendroff scheme [67], which is accurate to second order. Historically, the inclusion of an extra diffusion term,  $\gamma$ , has been used to ensure that a density function (i.e. a function that is non-negative by definition) remains positive, which is unconditionally enforced everywhere if  $\gamma = \frac{\beta'}{2}$ . In our case, the  $g_j^n$  include contributions from  $f_{i \geq 1}$ , which are expected to be negative in some regions of space. However, the presence of  $\gamma$  ensures the stability of  $g_j^{n+1}$ , which can be defined by the requirement that  $\Delta g_j^{n+1} < \max(\Delta g_{j-1}^n, \Delta g_j^n, \Delta g_{j+1}^n)$  where  $\Delta g_j^n = g_{j+1}^n - g_j^n$ . When the solution  $g_j^n$  is sharply varying or, in the extreme case, a discontinuity, the additional diffusion is necessary to suppress unphysical oscillatory behaviour in  $g_j^{n+1}$ .

**3. Anti-diffusion:** An ‘anti-diffusion’ step is employed to reduce the extra numerical diffusion introduced in (23) i.e.,

$$\bar{g}_j^{n+1} = g_j^{n+1} - \left( \gamma + \frac{\beta^2}{2} \right) (g_{j+1}^{n+1} - 2g_j^{n+1} + g_{j-1}^{n+1}). \quad (25)$$

The inclusion of this extra diffusion in step 2 assures that the solution is positive and physically realistic, and the straightforward application of step 3 undoes this which can re-introduce a negative solution. Boris and Book [68] suggested modifying the removal of the erroneous diffusion by just enough to maintain positivity, in a non-linear way (note that they worked with non-negative densities, as we have remarked on above in step 2). This is an early example and precursor of the modern technique of flux limiting [70–74]. In this work the full anti-diffusion step is applied in general, except in regions where a sharp variation or discontinuity is known *a priori* (e.g. configuration-space boundaries), in which case no anti-diffusion is applied. Unphysical oscillations can now occur, but we have found that for the situations considered they are negligibly small. The natural extension is to include flux limiting to prevent this unphysical behavior but this introduces extra computational complexity. The anti-diffusion step could also be solved implicitly rather than explicitly, but we found that this had no significant impact on the results.

It should be noted that the shift step can be performed after the advection and anti-diffusion stages with no change in the result. We have assumed that the boundaries are absorbing, in that the elements of  $g(t, z)$  that move outside the computational domain are lost, and no information is introduced from outside the domain. Although perfectly absorbing boundaries are notoriously difficult to implement numerically, in our calculations we avoid this problem by keeping the swarm density negligible at the simulation edges, through the use of an adaptive mesh, see Section III E. In practice we pre-calculate a transformation matrix (for a given set of parameters) which combines the above three steps for each of the grid energies.

### C. Energy-space advection and collisions

A major advantage of splitting the Boltzmann equation operator according to equations (12)-(13) is that  $S_U$  is then the familiar, spatially homogeneous Boltzmann equation.

There is much literature on solving this equation, and we use the approach developed previously [1, 75–77] to perform the numerical discretization and time-step. A full description of the numerical solution of the process is given in [77], and we will briefly summarize it here. The equation we need to solve is equation (13). The time dimension is discretized with a first order implicit Euler method, which has been chosen for its good stability properties. Similar to the work of Winkler and collaborators [78–80], we employ a finite difference method to discretize the system of ODE’s at centred points using a centred difference scheme, i.e.,

$$\left. \frac{df(U, t)}{dU} \right|_{U_{i+1/2}} = \frac{f(U_{i+1}, t) - f(U_i, t)}{U_{i+1} - U_i}, \quad (26)$$

$$f(U_{i+1/2}, t) = \frac{f(U_{i+1}, t) + f(U_i, t)}{2}, \quad (27)$$

so that equation (13) evaluated at  $i + 1/2$  becomes,

$$S_U(f_i)|_{i+1/2} = J_l(f_i)|_{i+1/2} + \left(\frac{2}{m}\right)^{\frac{1}{2}} \sum_{p=\pm 1} \Delta_i^{(p)} eE \left[ U_{i+1/2}^{\frac{1}{2}} \left( \frac{f_{l+p}(U_{i+1}, t) - f_{l+p}(U_i, t)}{U_{i+1} - U_i} \right) + p \frac{(l + \frac{3p+1}{2})}{2} U_{i+1/2}^{-\frac{1}{2}} \left( \frac{f_{l+p}(U_{i+1}, t) + f_{l+p}(U_i, t)}{2} \right) \right]. \quad (28)$$

Although a general form can be constructed for an arbitrary grid, the simplest case is for evenly spaced points, i.e.

$$U_i = i\Delta U \quad \text{for } 0 \leq i \leq n_U, \quad (29)$$

where  $\Delta U$  is a constant. By discretizing at the midpoint of the two solution nodes results in a system of linear equations that is under-determined. The extra information is naturally provided by boundary conditions which are appended to the system.

These boundary conditions have been analyzed by Winkler and collaborators [78–80] who investigated the multi-term, even order approximation, and discovered that the general solution of the steady-state hierarchy contains  $\frac{1}{2}(l_{\max} + 1)$  non-singular and  $\frac{1}{2}(l_{\max} + 1)$  singular fundamental solutions when  $U$  approaches infinity, and the physically relevant solution has to be sought within the non-singular set of fundamental solutions. The boundary conditions necessary for the determination of the non-singular physically relevant solution are [78]

$$\begin{aligned}
f_l(U = 0) &= 0 \text{ for odd } l, \\
f_l(U = U_\infty) &= 0 \text{ for even } l, \\
f_l(U > U_\infty) &= 0 \text{ for all } l,
\end{aligned} \tag{30}$$

where  $U_\infty$  represents a sufficiently large energy. In practice,  $U_\infty$  has to be determined in prior calculation, and is chosen such that the value of  $f_0(U_\infty)$  is less than  $10^{-10}$  of the maximum value of  $f_0$ .

#### D. Green's function solution

In our formalism and associated code, we solve for the Boltzmann equation Green's function

$$\mathcal{L}f_l = \delta(z - z_0)\delta(t - t_0), \tag{31}$$

where

$$\mathcal{L}f_l = \frac{\partial f_l}{\partial t} + \left(\frac{2}{m}\right)^{\frac{1}{2}} \sum_{p=\pm 1} \Delta_l^{(p)} \left[ U^{\frac{1}{2}} \frac{\partial}{\partial z} + \frac{eE}{m} \left( U^{\frac{1}{2}} \frac{\partial}{\partial U} + p \frac{(l + \frac{3p+1}{2})}{2} U^{-\frac{1}{2}} \right) \right] f_{l+p} + J_l(f_l) \tag{32}$$

for  $l = 0, 1, 2, \dots, \infty$ . The Green's function solution,  $f_l$ , can then be used to find the solution of the more general space-time Boltzmann equation, i.e.

$$\mathcal{L}\tilde{f}_l = S(z, t), \tag{33}$$

where  $S(z, t)$  is a source term, then

$$\tilde{f}_l(U, z, t) = \int dt_0 \int dz_0 f_l(U, z - z_0, t - t_0) S(z_0, t_0). \tag{34}$$

We do this by choosing an initial distribution in configuration-space that is a good approximation to a delta-function, which, for this study, is a narrow Gaussian,

$$\delta_a(z) = \frac{1}{a\sqrt{\pi}} \exp\left(-\frac{z^2}{a^2}\right), \tag{35}$$

where  $a$  is a parameter controlling the width of the Gaussian, representing the temporal-spatial relaxation profile of a single pulse centred on  $z_0$  and released at  $t_0$ . In the limit of

$a \rightarrow \infty$ ,  $\delta_a(z) \rightarrow \delta(z)$ . The formalism is quite general, enabling the treatment of various experiments (e.g. Pulsed Townsend (PT), Steady-State Townsend (SST) and other drift tube configurations [81] - detailed in Section III F), as well as various source and spatial/energy space/temporal distributions, through a single solution. This approach extends the functionality and accuracy of Boltzmann equation solutions to those routinely achieved by Monte Carlo simulations [47, 82, 83].

### E. Numerical considerations and adaptive meshing

The matrix system of linear equations that result from the discretization of the Legendre-decomposed Boltzmann equation in energy- and configuration-space at each time step are of the size  $(n_z n_U (l_{max} + 1)) \times (n_z n_U (l_{max} + 1))$ , where  $n_z$  and  $n_U$  are the number of nodes in configuration and energy space respectively. Due to the discretization schemes, the matrix is sparse and sparse techniques are employed to exploit this property. Each of these parameters are free to be increased until some convergence criterion is met. It should be noted that, although the two-term approximation ( $l_{max} = 1$ ) has been used extensively, it is well known that it can be insufficient in many situations [46].

In order to model the spatio-temporal relaxation of a narrow Gaussian source distribution in configuration-space with a distribution of energies as computationally efficiently as possible, we have developed a configuration-space node-mesh that adaptively follows the size of the distribution throughout the simulation. In this way a small configuration-space window is used around the original narrow Gaussian source which can then be sufficiently resolved with a small  $n_z$ . As the initial pulse drifts and diffuses, a small amount of information reaches and then leaks out of the window boundaries. Before the amount of information lost to the system exceeds some small tolerance, the window is extended and the solution at the previous time-step calculated on the new configuration-space mesh. We have found that the most convenient way to quantify the amount of information on the boundary is by the relative number density, and impose the condition that when

$$\int_{t_0}^t dt' \frac{n(z_L \text{ or } z_R, t')}{\int dz n(z, t')} \geq 10^{-5}, \quad (36)$$

then the configuration-space window is doubled (while the number of nodes is kept the same). Here  $t_0$  is the time of the last window adjustment,  $z_L$  and  $z_R$  are locations of the left

and right configuration-space boundaries respectively. The choice to extend the window by doubling is to make it so that the new mesh lines up exactly with nodes of the old mesh, hence requiring no interpolation. The accuracy of the modified Lax-Wendroff scheme used to model the configuration-space advection [67] is related to the parameter  $\beta = \frac{\Delta t}{\Delta z} \Lambda$ , hence by doubling  $\Delta z$  after a re-adjustment, the value of  $\Delta t$  can also be doubled. This effectively allows us to use smaller time steps when our solution is sharp and diffusing quickly, and larger time steps once the solution has spread out and is varying less quickly. A maximum value for the time step size still needs to be enforced however, since with bigger time step sizes less mixing between the configuration-space and energy-space components of the operator splitting occurs, leading to errors.

There is one extra complication to be discussed. Since the boundaries are absorbing, when they are re-adjusted, the number density profiles (and distribution functions) drop directly from the built-up value at the previous boundaries location to zero in a single  $\Delta z$ , which can lead to problematic, unphysical, oscillatory solutions when treated with the method described in Section III B. In order to combat this, we simply apply the procedure without the final anti-diffusion step for a small amount of time on the edge and in the newly opened regions. The extra diffusion added ensures that the solution remains positive and give physical results, which, after a small amount of time, ensures that the profiles decrease smoothly to zero at the boundary. After this short correction time, we again apply the full procedure. By not removing the added extra diffusion we have increased the overall diffusion, but since it is only applied for a small time and to a region where there is necessarily only a small proportion of particles, this does not significantly affect the transport profiles.

## F. Transport properties

The cross-sections and collision operator terms represent the microscopic picture of electron interactions with the medium. The macroscopic picture, e.g. transport properties that represent experimental measurables, are obtained as averages of certain quantities with respect to the distribution function,  $f$ . Among the transport properties of interest in the current manuscript are the number density,  $n$ , particle flux,  $\Gamma$ , and average energy,  $\epsilon$ , of the electron swarm, which can be calculated via

$$n(z, t) = 2\pi \left(\frac{2}{m}\right)^{\frac{3}{2}} \int dU U^{\frac{1}{2}} f_0(U, z, t), \quad (37)$$

$$\Gamma(z, t) = \frac{2\pi}{3} \left(\frac{2}{m}\right)^2 \int dU U f_1(U, z, t), \quad (38)$$

$$\epsilon(z, t) = \frac{1}{n(z, t)} 2\pi \left(\frac{2}{m}\right)^{\frac{3}{2}} \int dU U^{\frac{3}{2}} f_0(U, z, t). \quad (39)$$

Likewise, we can sample the traditional hydrodynamic transport coefficients in this non-hydrodynamic framework, e.g. the drift velocity,  $W$ , and the (longitudinal) diffusion coefficient,  $D_L$ :

$$W(t) = \frac{d}{dt} \left[ \frac{1}{N(t)} \left( \int dz z n(z, t) \right) \right], \quad (40)$$

$$D_L(t) = \frac{1}{2} \frac{d}{dt} \left[ \frac{1}{N(t)} \left( \int dz z^2 n(z, t) \right) - \left( \frac{1}{N(t)} \int dz z n(z, t) \right)^2 \right], \quad (41)$$

where  $N(t)$  is the total number of particles:

$$N(t) = \int dz n(z, t). \quad (42)$$

When the above properties are calculated from the Green's function solution, which corresponds to a simulation of a PT experiment, then the transport properties for other experimental systems can also be calculated in a straightforward manner. In this work we are also interested in the results of a SST simulation, for which there have been previous calculations performed for benchmark systems. Similar to [23, 27, 47], the SST transport properties can be determined from the Green's function transport properties via

$$f_i^{SST}(U, z) = \int_0^\infty dt_0 f_i(U, z, t_0), \quad (43)$$

$$n_{SST}(z) = \int_0^\infty dt_0 n(z, t_0), \quad (44)$$

$$\Gamma_{SST}(z) = \int_0^\infty dt_0 n(z, t_0) v_z(z, t_0), \quad (45)$$

$$\epsilon_{SST}(z) = \frac{1}{n_{SST}(z)} \int_0^\infty dt_0 n(z, t_0) \epsilon(z, t_0). \quad (46)$$

In practice the upper limit of the integrals is not  $\infty$ , but a sufficiently long time for the SST transport properties to have converged over the  $z$  range considered.



### G. Reduced variables

Henceforth, it is convenient to work with rescaled reduced variables. In particular, the space and time variations will be presented as functions of

$$z^* = n_0\sigma_0z, \quad (47)$$

$$t^* = n_0\sigma_0\sqrt{\frac{2e}{m}}t, \quad (48)$$

where  $\sigma_0 = 10^{-20}$  m<sup>2</sup>. Likewise, the electric field dependence arises through the reduced electric field  $E/n_0$  in units of Townsend (1 Td = 10<sup>-21</sup>Vm<sup>2</sup>). By presenting results in this manner scales out the  $n_0$  dependence, and hence allows comparisons between the dilute gas phase and the liquid/dense gas phase, to give a true reflection of the impact of coherent and other scattering effects.

## IV. ELECTRON TRANSPORT IN A MODIFIED PERCUS-YEVICK HARD-SPHERE BENCHMARK LIQUID MODEL

In order to investigate the effects of medium structure on charged particle transport, a model for the structure function is required. One such model, frequently employed in the literature, is that of a structure for a system of hard-sphere potentials obtained by applying the Percus-Yevick approximation as a closure to the Ornstein-Zernike equation, which yields a pair-correlation function [84, 85]. The static structure factor is found via the Fourier transform of the pair-correlation function, the angle-integration of which is used directly in the numerical simulations. In particular, we use the model of Percus and Yevick with the Verlet-Weiss correction [86, 87] to better emulate the structure of a real liquid (see [83] for details). The volume fraction parameter,  $\Phi$ , specifies how tightly packed the hard spheres in the medium are. It can be written in terms of the hard-sphere radius  $r$  and the neutral number density,  $n_0$ , as  $\Phi = \frac{4}{3}\pi r^3 n_0$ . Smaller volume fractions indicate a larger interparticle spacing, and vice versa. We have modeled systems with a range of densities, from  $\Phi \approx 0$ , which approximates a dilute gas, to  $\Phi = 0.4$ , which states that 40% of the volume is excluded by hard-sphere potentials of the neutral molecules. Differences in the results highlight the importance of coherent elastic scattering.

The remaining details required of the benchmark hard-sphere model implemented for

electron sized particles are

$$\begin{aligned}
 \sigma_m &= 6 \text{ \AA}^2, \\
 \sigma^{\text{exc}} &= \begin{cases} 0, & U < 2 \text{ eV} \\ 0.1 \text{ \AA}^2, & U \geq 2 \text{ eV} \end{cases} \\
 \Phi &= 0, 0.2, 0.3, 0.4, \\
 E/n_0 &= 3 \text{ Td}, \\
 m_0 &= 4 \text{ amu}, \\
 T_0 &= 0 \text{ K}.
 \end{aligned} \tag{49}$$

A step-like inelastic process has been included in addition to the standard Percus-Yevick hard sphere benchmark system in model (49). The inelastic channel introduces a periodic oscillatory non-hydrodynamic behaviour, similar to those observed in the well-known Frank-Hertz experiment, and can hence determine whether the numerical code is accurately capturing the non-hydrodynamic phenomena. Figure 1 highlights the variation of the momentum transfer cross-section with  $\Phi$ , evaluated using the cross-section in (49) together with the static structure factor from [83]. At high energies, coherent scattering effects are suppressed, and the various momentum transfer cross sections converge on the dilute gas case (corresponding to  $\Phi = 0$ ).

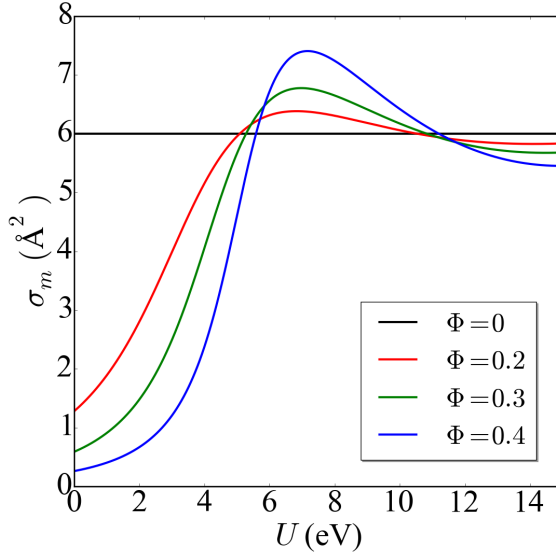


Figure 1: The variation of the elastic momentum-transfer cross-section including structure with energy for model (49) for various volume fractions,  $\Phi$ .

The source distribution is given by

$$f(U, z, 0) = Af_U(U)f_z(z), \quad (50)$$

where  $f_z(z)$  is a narrow Gaussian in configuration-space, i.e.,

$$f_z(z) = \frac{1}{\Delta z_0 \sqrt{2\pi}} \exp\left(-\frac{1}{2} \left(\frac{z}{\Delta z_0}\right)^2\right), \quad (51)$$

(we take  $\Delta z_0 = 0.1$ ), while  $f_U(U)$  corresponds to drifted Maxwellian distribution with  $T = 10^5$  K, and  $\mathbf{W} = 10^4 \text{ ms}^{-1} \hat{\mathbf{E}}$ , i.e.,

$$f(\mathbf{v}) = n \left(\frac{m}{2\pi kT}\right)^{(3/2)} \exp\left[-\frac{m}{2k_b T} (\mathbf{v} - \mathbf{W})^2\right], \quad (52)$$

and  $A$  is a normalization constant such that  $\int U^{1/2} f(U, z, 0) dU = 1$ .

### A. Transport coefficients in the long-time limit

The asymptotic values of the drift velocity and diffusion coefficient calculated from the spatial moments (40) and (41) respectively using the full non-hydrodynamic code are displayed in Table I for various volume fractions. Here we compare these values with those

determined from a purely hydrodynamic formalism and associated code [1, 77]. The first order hydrodynamic transport coefficients, i.e., the mean energy and drift velocity, agree to within 0.2% with the asymptotic non-hydrodynamic values for the volume fractions considered. The hydrodynamic and non-hydrodynamic calculations of the longitudinal diffusion coefficient agree to within 0.7%. As the volume fraction increases, both the mean energy, drift velocity and diffusion coefficient increase monotonically, a consequence of the coherent scattering, where at low energies, increasing volume fractions leads to decreasing structure factors at low  $\Delta k$ , and hence decreased momentum-transfer cross-sections. For further discussion on the physical variation of the hydrodynamic transport coefficients with volume fraction the reader is referred to [50, 83, 88].

Table I: Comparison of the transport quantities calculated from non-hydrodynamic (first row) and time asymptotic hydrodynamic (second row) formalisms for model (49) at various volume fractions  $\Phi$ .

$\Phi$	$\epsilon$ [eV]	$W$ [ $10^4 \text{ m s}^{-1}$ ]	$n_0 D_L$ [ $10^{24} \text{ m}^{-1} \text{ s}^{-1}$ ]
0	0.8335	1.385	2.386
	0.8337	1.385	2.387
0.2	0.9765	3.397	6.333
	0.9772	3.391	6.328
0.3	1.080	5.929	11.22
	1.080	5.921	11.24
0.4	1.233	10.52	19.51
	1.233	10.51	19.63

## B. Space-time evolution of the phase-space distribution and its velocity moments

In Figure 2 the space-time evolution of the  $f_0$  and  $f_1$  velocity distribution function components are compared for  $\Phi = 0$  and  $\Phi = 0.4$  at three different times. The space-time evolution of the integral moments of  $f_0$ , electron density  $n(z, t)$ , and velocity moment of  $f_1$ , the flux  $\Gamma$ , are displayed in Figure 3. The timescale for variation of  $f_0$  is governed by  $\sim \left(2 \frac{m}{m_0} \nu_m\right)^{-1}$ ,

and hence there is no explicit  $\Phi$  dependence in the timescale, however differences arise due to the implicit energy dependence in the collision frequency (which does depend on  $\Phi$ ) and the coupling to higher order moments with different timescales. The timescale for variation of  $f_1$  on the other hand is governed by  $\tilde{\nu}_m^{-1}$ , which has an explicit  $\Phi$  dependence. The timescale for momentum exchange is significantly decreased for increasing  $\Phi$  at low energies, as shown in Figure 1, however they approach the same value at higher energies. We will show that this is reflected in the evolution of the profiles.

At small times (e.g.  $t^* = 0.2$ ), there are only small differences in the  $f_0$  contours between the two volume fractions, and this is also highlighted in the density  $n(z, t)$ . At higher energies ( $> 5-6$  eV) there are also very little differences in the  $f_1$  contours (reflecting the similarity in the momentum relaxation times at these energies), however at low energies, the  $\Phi = 0.4$  contours for  $f_1$  are significantly displaced in both energy and configuration-space relative to the  $\Phi = 0$  case. This indicates significantly higher advective and diffusive fluxes in this energy regime at this time, which is evidenced in the flux profiles of Figure 3. Given the sharp initial pulse with large spatial gradients, we observe large positive and negative diffusive fluxes, along with a large positive advective contribution.

At larger times, the  $f_0$  and  $f_1$  contours in the  $\Phi = 0.4$  case depart significantly from the  $\Phi = 0$  case, initially in the low energy regime and then finally the entire energy regime as the higher energy electrons relax from the initial condition. The peaks in each of the distribution components at larger times for  $\Phi = 0.4$  case are significantly displaced in the  $z$ -direction from the  $\Phi = 0$  case. This is reflected in both the density and flux profiles at larger times, which highlight the enhanced drift and diffusion due to the reduced momentum transfer cross-section associated with coherent scattering for this model and field. Interestingly, at sufficiently long times, the  $\Phi = 0.4$  contours have predominantly positive values, and only very small negative excursions at low energies, in contrast to the  $\Phi = 0$  contours. At these times, the flux is positive over the swarm indicating that the advective contribution dominates the diffusion contribution, since the density gradients are much more rapidly dissipated in the  $\Phi = 0.4$  case, see Figure 3.

Strikingly, both the  $\Phi = 0$  and  $\Phi = 0.4$  contours for both  $f_0$  and  $f_1$  demonstrate periodic structures in both configuration space and in energy space at sufficiently long times and sufficiently downstream from the source. The periodic structures manifest themselves earlier for the  $\Phi = 0.4$  case. These are the well known Franck-Hertz oscillations [26, 27]. A

simplistic picture of this non-hydrodynamic phenomena is that the electrons in the swarm are being repeatedly accelerated by the electric field to an energy above the inelastic process threshold whereby they undergo an inelastic collision losing their energy. This simple physics is evidenced in the  $f_0$  and  $f_1$  distributions. By integrating over the energy to obtain the density and flux, shown in Figure 3, much of the periodic structures observed in the distribution function is masked, however some non-Gaussian spatial structure is still observed. We will explore the  $\Phi$ -dependence of the wavelengths of oscillations further in Section IV C.

### C. Steady-state Townsend configuration

The solution detailed in Section IV B is essentially equivalent to solving for the Boltzmann equation Green's function for the model (49). A strict validation of this approach and associated numerical code is to be able to reproduce the Steady-State Townsend (SST) transport properties from the Green's function solution, as described in Section III D. The average energy (46) and average velocity (45) for SST simulations of various volume fractions are shown in Figure 4. In the spatially asymptotic regime, the average energy and the average velocity are equal to the hydrodynamic and pulsed-Townsend values shown in Table I. It can be seen that the SST properties demonstrate damped spatially periodic structures similar to those observed in the Frank-Hertz experiment and other investigations [26, 27, 31, 89–91]. They are a manifestation of the energy and space periodic structures in the distribution function components, and in the spatially periodic structures in the density and flux profiles of Figure 3. By assuming the elastic scattering is weak, the width between the peaks in the transport property profiles,  $\lambda$ , is directly related to the threshold energy of the inelastic process,  $U_I$  in eV, via [92]

$$\lambda = \frac{U_I}{(0.1)_{eV/Td} (E/n_0)_{Td}}, \quad (53)$$

where the reduced electric field is in Townsend (Td). For model (49), the theoretical spacing is 6.6. In Figure 4 it is possible to see that there are variations in the wavelength of the spatial structures with  $\Phi$ , as well as significant differences in the decay rates of the oscillation amplitudes. For  $\Phi = 0$ , the wavelength is approximately  $8.24 \pm 0.02$  and this decreases to  $6.67 \pm 0.02$  for  $\Phi = 0.4$ . The differences arise explicitly due the differences in the elastic momentum transfer cross-section, as well as implicit variations associated with the modification to the swarm's energy with  $\Phi$ . For  $\Phi = 0.4$ , the momentum transfer cross-

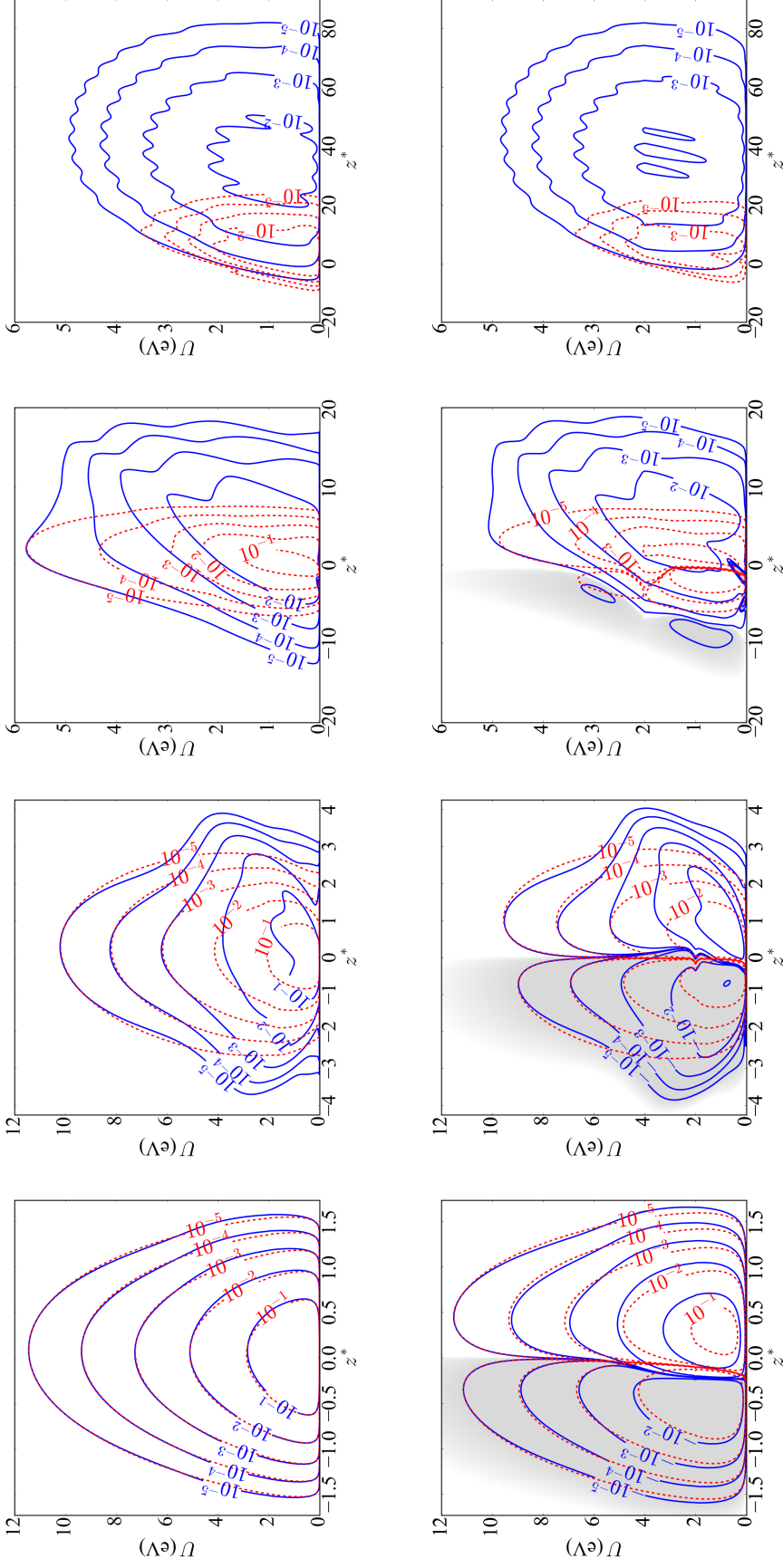


Figure 2: Temporal evolution of the distribution function components for model (49) with  $\Phi = 0$  (dashed lines) and  $\Phi = 0.4$  (solid lines). The first row are  $U^{1/2} f_0/n_0$  ( $\text{eV}^{-1}$ ) contours while the second row are  $|U f_1/n_0|(\text{eV}^{-1/2})$  contours. The shaded contours indicate  $U f_1 < 0$ . The four columns represent the times,  $t^* = 0.2, 2, 20$ , and  $200$  respectively.

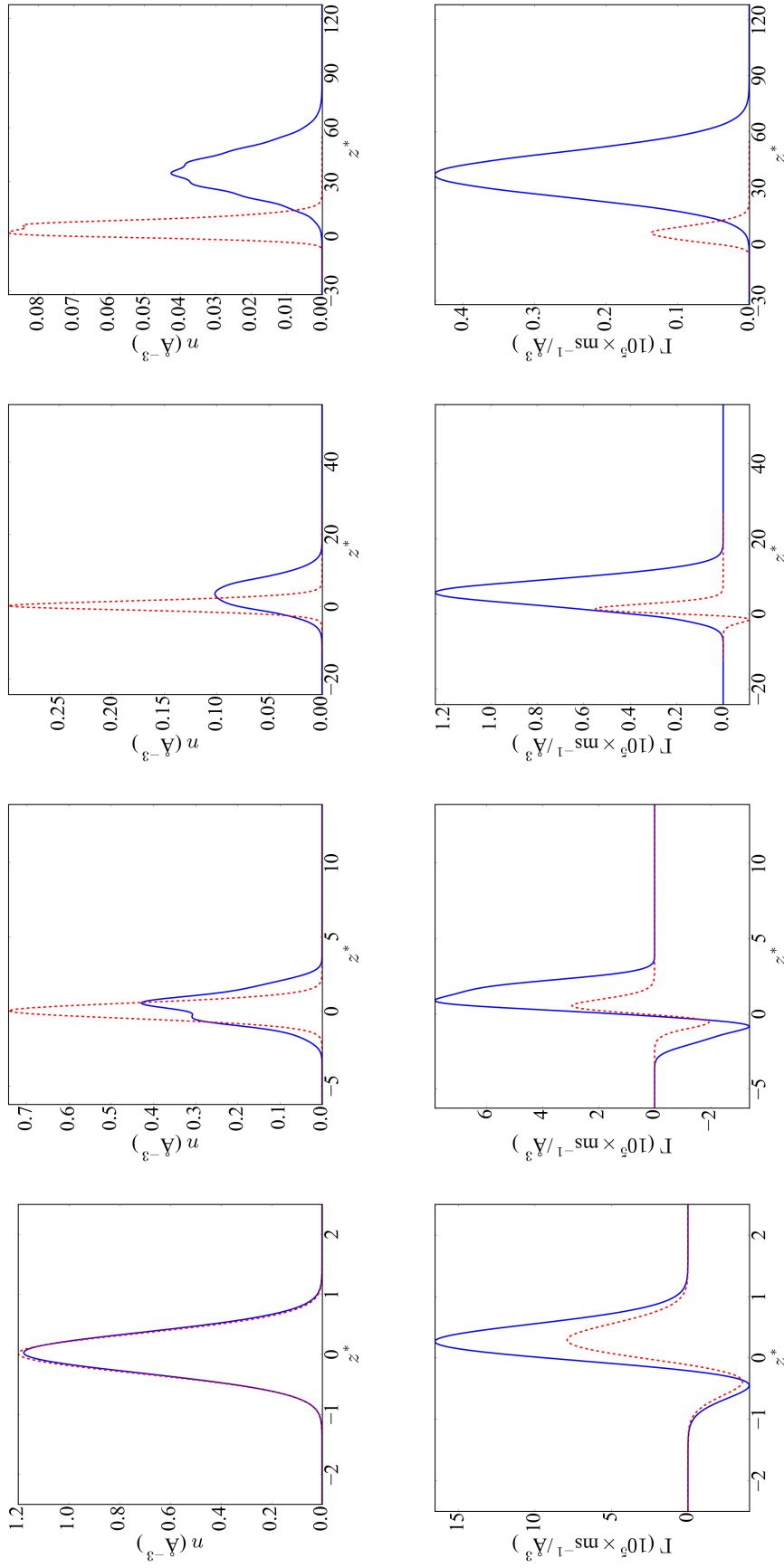


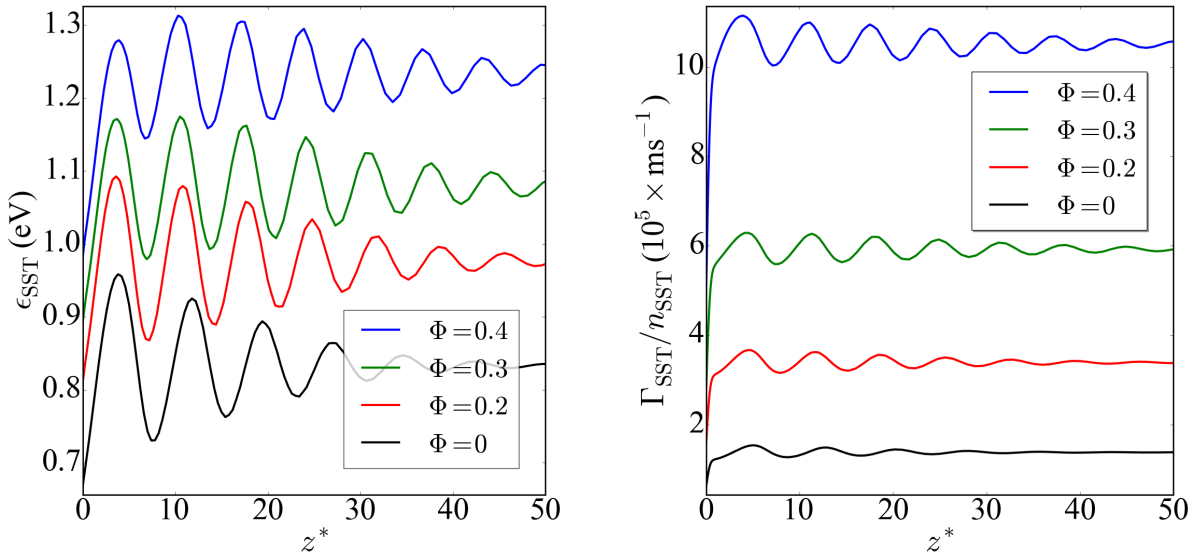
Figure 3: Temporal evolution of the spatially varying density and flux for model (49) with  $\Phi = 0$  (dashed lines) and  $\Phi = 0.4$  (solid lines). The four columns represent the times,  $t^* = 0.2, 2, 20,$  and  $200$  respectively.



section for elastic scattering is significantly reduced compared to the  $\Phi = 0$  case. Hence, the randomizing collisions that dampen the oscillations [27] are reduced for  $\Phi = 0.4$  as compared to other  $\Phi$ , and the variation of damping with  $\Phi$  then follows. Likewise, it should not be surprising that the wavelength for the  $\Phi = 0.4$  case is closest to the analytic value of (53), since the reduced momentum transfer associated with the  $\Phi = 0.4$ , more closely approximates the weak elastic scattering assumption used in deriving it.

We must also point out that the validity of these profiles are dependent on the discretization of the distributions in configuration-space. If the spatial discretization is of the same order as the Frank-Hertz wavelength, then it will be very difficult to resolve these features in the distributions and consequently the time-averaged profiles. Of course, our initial choice for the discretization is small enough to easily resolve these features, but as the simulation progresses and the distribution diffuses, our adaptive mesh will increase in range and also increase the spatial discretization step size. After a point, the coarseness of the discretization causes the distribution to slowly lose its features, which is visible in the time-averaged quantities by the suppression of the amplitude of the oscillations. In our simulations we expect our results for  $z^* \gtrsim 30$  deviate from the true spatially dependent steady-state values, however the fully relaxed values agree with the hydrodynamic values. It is simple to address this issue by increasing the number of points in configuration-space but this is also significantly more computationally intensive.

Figure 4: Spatial variation of the average energy and average velocity under SST conditions for model (49) with various volume fractions  $\Phi$ .



## V. SPATIO-TEMPORAL RELAXATION OF ELECTRONS IN LIQUID ARGON

Electron transport in liquid argon is an essential component in the function of Liquid Argon Time Projection Chambers (LArTPC) which are currently being used for high energy particle detection [5]. Ionized electrons in liquid argon originating from the high energy particles are accelerated under the action of an electric field to generate a current and consequently reconstruct the path of the high energy particle. Typically these chambers operate with electric field strengths of less than 500 kV/cm. The aim of this component is to follow the spatio-temporal evolution of these ionized electrons in liquid argon, relevant to the operation of these detectors. Foxe et al. [93] have measured the energy distribution of the electrons ionized by high energy particles in liquid argon, and have shown that the majority of the ionized electrons have energies below 1 eV. Consequently in this study we employ an initial source energy-distribution that is constant in energy space up to 1 eV, i.e.,

$$f_U(U) = CU^{-1/2}\Theta(U - 1\text{ eV}), \quad (54)$$

where  $\Theta$  is the Heaviside step function, and  $U$  is in eV and  $C$  is a normalisation constant. The mean energy of this distribution is 0.5 eV. The swarm is released from a narrow Gaussian

in configuration-space,

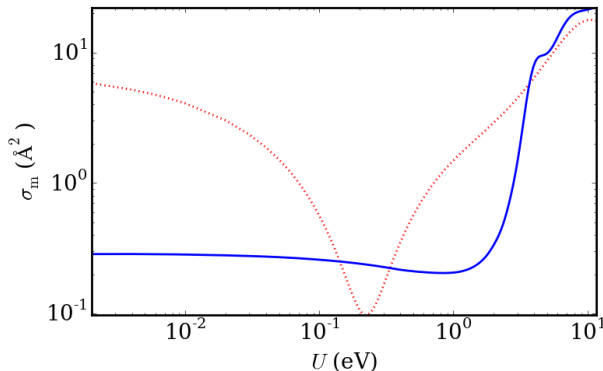
$$f_z(z) = \frac{1}{\Delta z_0 \sqrt{2\pi}} \exp\left(-\left(\frac{z}{\Delta z_0}\right)^2\right) \quad (55)$$

so that the full initial phase-space distribution is  $f(U, z, 0) = Af_U(U)f_z(z)$ , where  $A$  is a normalization constant such that  $\int U^{1/2} f(U, z, 0) dU = 1$ . For argon, we take  $\Delta z_0 = 10$ , a larger initial spread than for the Percus-Yevick model, reflecting the smaller cross-sections of argon.

### A. Cross-sections, potentials and screening

In a recent paper [1] we investigated the modifications required to treat transport of electrons in dense gaseous and liquid argon, with our simulations focused purely on the hydrodynamic regime. The work followed closely the approach of Lekner and Cohen [2, 3] updated using modern scattering theory techniques, theories, potentials etc. The potentials, screening factor, and cross-sections derived in [1] are used once again here, and we briefly summarize the process. The gas-phase elastic scattering cross-sections were calculated by solving the Dirac-Fock scattering equations [94], and were shown to give good agreement with both beam scattering cross-sections and swarm experimental drift velocities and characteristic energies. As the medium's density increased, density effects became important. The effects of the high density of the liquid are included in our calculations through several modifications of the gas-phase scattering properties, and are dependent on the liquid argon pair-correlation function and associated static structure factor [95]. The first modification is to account for the screening of a single induced atomic dipole by the induced dipoles of all other atoms. In a high density medium, the potential produced by the induced multipole moments is of a sufficiently long enough range to interact with induced multipole moments by other atoms in the bulk. The second modification is to construct an effective potential in which there are contributions from both the target atom and the surrounding bulk, the latter of which is done as an ensemble average. The momentum transfer cross-sections calculated from the dilute gaseous and liquid argon potentials are shown in Figure 5. It is significant to note the absence of the Ramsauer minimum in the liquid-phase cross-section.

Figure 5: The momentum transfer cross-sections in the gas-phase (dashed line) and liquid-phase (solid line) for electrons in argon [1].



## B. Results

To consider conditions representative of those in liquid state particle detectors, we simulate electron transport in liquid argon under the following conditions:

$$\begin{aligned}
 E/n_0 &= 2.5 \times 10^{-3} \text{ Td}, \\
 T &= 85 \text{ K}, \\
 m_0 &= 40 \text{ amu}.
 \end{aligned}
 \tag{56}$$

The reduced field is equivalent to 500 kV/cm with a density corresponding to liquid argon,  $n_0 = 0.0213 \text{ \AA}^{-3}$ . For this reduced electric field and source distribution, given in (54)-(55), the electron swarm energies are generally well below the first inelastic channel threshold energy (8.9 eV), so that there is no inelastic channel operative, and hence the periodic spatial structures observed in the Percus-Yevick hard-sphere liquid model above are not present.

The relaxation of the  $f_0$  distribution function component are compared for the gas and liquid phases at three different times in Figure 6. At  $t^* = 1$ , there are only small differences between the contours reflecting similar energy relaxation rates between the two phases initially. At  $t^* = 10$ , a bulge is beginning to develop in the gas-phase contour in the energy region between 0.1 – 0.5 eV, which corresponds to the Ramsauer minimum in the gas-phase momentum transfer cross-section. In this region, the gas-phase momentum transfer cross-section dips below the liquid cross-section, which has resulted in this enhancement of the

diffusive flux in this range. At higher energies the liquid cross-section is less than the gas-phase cross-section, which has resulted in enhanced diffusive flux. At  $t^* = 100$  these effects are even more pronounced.

In Figure 6 the  $f_1$  component contours for the gas and liquid phases of argon are compared for the same three times. At the first time,  $t^* = 1$ , there is already significant differences in the  $f_1$  contours, with the largest change occurring in the Ramsauer minimum range in the gas-phase case. This highlights again the difference in the timescales of the energy and momentum relaxation between the two phases. As time increases, greater differences develop between the  $f_1$  contours particularly around the Ramsauer minimum and at the high energy range for the reasons previously discussed.

The number density as a function of time is shown in Figure 6. The behavior of the number density profiles is consistent with the behaviour of the  $f_0$  and  $f_1$  profiles. At  $t^* = 1$  there is no noticeable difference in the two number density profiles. At later times it is clear that, despite the Ramsauer minimum in the gas-phase, the liquid-phase experiences the greater diffusion rate overall. For the electric field considered and initial source distribution, the average drift velocity for both the gas and liquid phases is small compared to the diffusion rates.

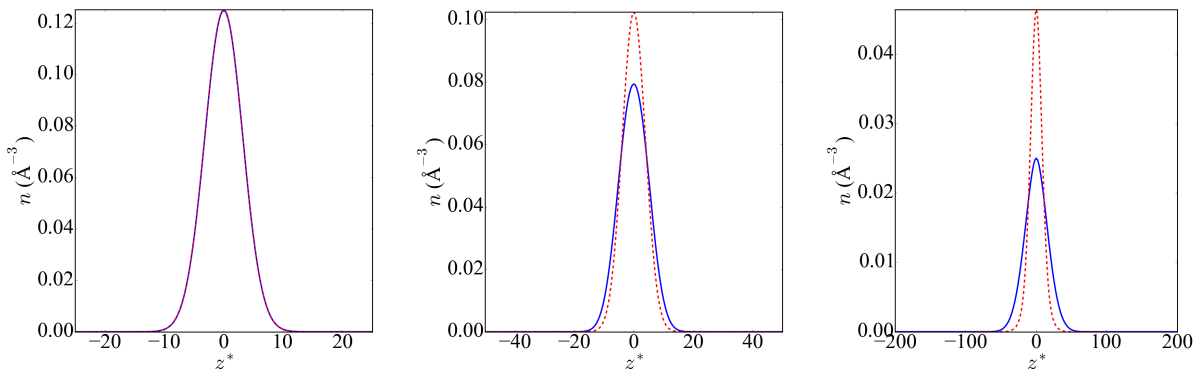


Figure 7: Temporal evolution of the number density profiles for gas-phase (dashed lines) and liquid-phase (solid lines) argon. The three columns represent the times,  $t^* = 1$ , 10, and 100 respectively.

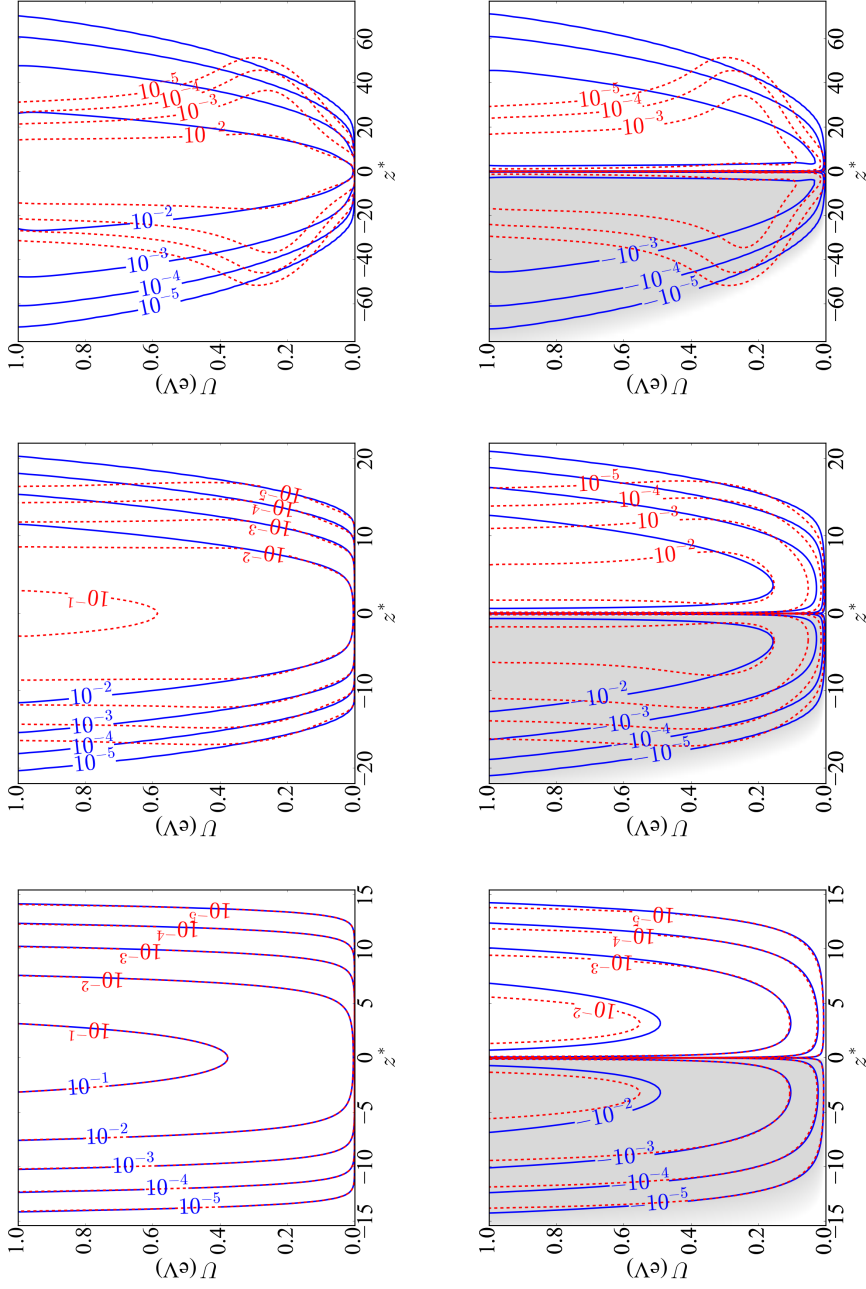


Figure 6: Temporal evolution of the distribution function components for gas-phase (dashed lines) and liquid-phase (solid lines) argon. The first row are  $U^{1/2} f_0 / n_0 (\text{eV}^{-1})$  contours, the second row are  $|U f_1 / n_0| (\text{eV}^{-1/2})$  contours. The shaded contours indicate  $U f_1 < 0$ . The three columns represent the times,  $t^* = 1, 10$ , and  $100$  respectively.

$U f_1 < 0$ . The three columns represent the times,  $t^* = 1, 10$ , and  $100$  respectively.

## VI. CONCLUSION

We have developed a full multi-term, space-time dependent solution of the electron Boltzmann equation in gases and liquids capable of modeling non-hydrodynamic conditions. The flexibility of the algorithm lies in solving the Boltzmann equation's Green's function, knowledge of which allows one to construct the solution for other experimental configurations e.g. the SST experiment and similar applications. Operator splitting has been employed to efficiently evolve the energy-space and configuration-space components individually with tailored numerical schemes.

The theory and associated code was first applied to a simple hard-sphere benchmark model liquid, where structure effects were simulated by the Percus-Yevick structure factor as a function of the volume fraction,  $\Phi$ . The inclusion of an inelastic channel was a key test of the algorithm's ability to reproduce non-hydrodynamic phenomena. Periodic spatial structures developed in the space-time and steady-state profiles for the distribution function components and associated transport properties, the periodicity of which is directly related to the threshold energy of the inelastic process. We observed that these periodic structures arose on shorter times scales when coherent scattering effects became important. The steady-state profiles constructed for various volume fractions also reproduced the non-hydrodynamic oscillatory structures expected. The asymptotic transport coefficients calculated from the non-hydrodynamic solution of Boltzmann's equation were also shown to be consistent with the values calculated from a hydrodynamic solution of Boltzmann's equation.

Finally, the cross-sections calculated in [1] were used to investigate the spatio-temporal evolution of electrons in gas-phase and liquid-phase argon. The two momentum-transfer cross-sections feature different qualitative and quantitative behaviours. Striking differences in the evolution of the components of the phase-space distribution were apparent, reflecting the differences in the gas-phase and liquid-phase cross-sections, particularly the absence of a Ramsauer minimum in the liquid-phase. This highlights the problems associated with treating liquid systems as gaseous systems with increased density, which has implications for various applications including liquid argon time projection chambers.

## ACKNOWLEDGMENTS

This work was supported under the Australian Research Council's (ARC) Centre of Excellence and Discovery programs.

---

- [1] G. J. Boyle, R. P. McEachran, D. G. Cocks, and R. D. White, *J. Chem. Phys.* **142**, 154507 (2015).
- [2] J. Lekner, *Phys. Rev.* **158**, 130 (1967).
- [3] M. H. Cohen and J. Lekner, *Phys. Rev.* **158**, 305 (1967).
- [4] W. Schmidt, *Liquid state electronics of insulating liquids* (CRC Press, Boca Raton, 1997).
- [5] A. Marchionni, *Annual Review of Nuclear and Particle Science* **63**, 269 (2013).
- [6] E. Aprile, K. Arisaka, F. Arneodo, A. Askin, L. Baudis, A. Behrens, K. Bokeloh, E. Brown, J. M. R. Cardoso, B. Choi, et al. (XENON100 Collaboration), *Physical Review Letters* **105**, 131302 (2010).
- [7] E. Aprile, J. Angle, F. Arneodo, L. Baudis, A. Bernstein, A. Bolozdynya, P. Brusov, L. C. C. Coelho, C. E. Dahl, L. DeViveiros, et al., *Astroparticle Physics* **34**, 679 (2011), 1001.2834.
- [8] T. Sumner, *New Astronomy Reviews* **49**, 277 (2005).
- [9] M. G. Kong, G. Kroesen, G. Morfill, T. Nosenko, T. Shimizu, J. van Dijk, and J. L. Zimmermann, *New J. Phys.* **11**, 115012 (2009).
- [10] W. Tian and M. J. Kushner, *J. Phys. D* **47**, 165201 (2014).
- [11] S. A. Norberg, W. Tian, E. Johnsen, and M. J. Kushner, *J. Phys. D* **47**, 475203 (2014).
- [12] C. Chen, D. X. Liu, Z. C. Liu, A. J. Yang, H. L. Chen, G. Shama, and M. G. Kong, **34**, 403 (2014).
- [13] Y. Zheng, J. R. Wagner, and L. Sanche, *Phys. Rev. Lett.* **96**, 208101 (2006).
- [14] A. M. Munoz, C. Fuss, M. A. Cortes-Giraldo, S. Incerti, V. Ivanchenko, A. Ivanchenko, J. M. Quesada, F. Salvat, C. Champion, and G. Garcia, *Monte Carlo Methods to Model Radiation Interactions and Induced Damage* (Springer, New York, 2012).
- [15] R. White, J. Sullivan, A. Bankovic, S. Dujko, R. Robson, Z. L. Petrovic, G. Garcia, M. Brunger, and S. Buckman, *Positron and Electron Interactions and Transport in Biological Media: Modeling Tracks and Radiation Damage* (Springer, New York, 2012).



- [16] H. Nikjoo, D. Emfietzoglou, R. Watanabe, and S. Uehara, *Radiation Physics and Chemistry* **77**, 1270 (2008).
- [17] G. J. Boyle, R. P. McEachran, D. G. Cocks, and R. D. White, *The Journal of Chemical Physics* **142**, 154507 (2015), ISSN 0021-9606, URL <http://scitation.aip.org/content/aip/journal/jcp/142/15/10.1063/1.4917258>.
- [18] R. E. Robson and K. F. Ness, *Phys. Rev. A* **33**, 2068 (1986).
- [19] R. D. White, K. F. Ness, R. E. Robson, and B. Li, *Phys. Rev. E* **60**, 2231 (1999).
- [20] R. D. White, K. F. Ness, and R. E. Robson, *Applied Surface Science* **192**, 26 (2002).
- [21] R. D. White, R. E. Robson, S. Dujko, P. Nicoletopoulos, and B. Li, *J. Phys. D: Appl. Phys.* **42**, 194001 (2009).
- [22] D. Loffhagen and F. Sigeneger, *Plasma Sources Sci. Technol.* **18**, 034006 (2009).
- [23] B. Li, R. D. White, and R. E. Robson, *J. Phys. D: Appl. Phys.* **35**, 1 (2002).
- [24] I. A. Porokhova, Y. B. Golubovskii, J. Bretagne, M. Tichy, and J. F. Behnke, *Phys. Rev. E* **71**, 066406 (2005).
- [25] I. A. Porokhova, Y. B. Golubovskii, J. Bretagne, M. Tichy, and J. F. Behnke, *Phys. Rev. E* **71**, 066407 (2005).
- [26] J. Frank and G. Hertz, *Verh. Deutsche Phys. Ges.* **16**, 457 (1914).
- [27] R. E. Robson, B. Li, and R. D. White, *J. Phys. B: At. Mol. Opt. Phys.* **33**, 507 (2000).
- [28] R. Winkler and F. Sigeneger, *J. Phys. D: Appl. Phys.* **34**, 3407 (2001).
- [29] R. Winkler, F. Sigeneger, and D. Uhrlandt, *Pure Appl. Chem.* **68**, 1065 (1996).
- [30] F. Sigeneger and R. Winkler, *Plasma Chemistry and Plasma Processing* **17**, 1 (1997).
- [31] F. Sigeneger and R. Winkler, *Plasma Chemistry and Plasma Processing* **17**, 281 (1997).
- [32] R. Winkler, G. Petrov, F. Sigeneger, and D. Uhrlandt, *Plasma Sources Sci. Technol.* **6**, 118 (1997).
- [33] D. Loffhagen, F. Sigeneger, and R. Winkler, *Plasma Process.* **18**, 153 (2003).
- [34] F. Sigeneger, Y. B. Golubovskii, I. A. Porokhova, and R. Winkler, *Plasma Chem. and Plasma Process.* **20**, 429 (1998).
- [35] F. Sigeneger and R. Winkler, *Plasma Chem. and Plasma Process.* **20**, 429 (2000).
- [36] F. Sigeneger, G. I. Sukhinin, and R. Winkler, *Plasma Chem. and Plasma Process.* **20**, 87 (2000).
- [37] Y. B. Golubovskii, R. V. Kozakov, V. A. Maiorov, J. Behnke, and J. F. Behnke, *Phys. Rev. E*

- 62**, 2707 (2000).
- [38] Y. B. Golubovskii, A. Y. Skoblo, V. A. Maiorov, and V. O. Nekutchayev, *Plasma Sources Sci. Technol.* **11**, 309 (2002).
- [39] Y. B. Golubovskii, I. A. Porokhova, J. Behnke, and V. O. Nekutchayev, *J. Phys. D: Appl. Phys.* **31**, 2447 (1998).
- [40] Y. B. Golubovskii, V. A. Maiorov, I. A. Porokhova, and J. Behnke, *J. Phys. D: Appl. Phys.* **32**, 1391 (1999).
- [41] B. Li, R. E. Robson, and R. D. White, *Phys. Rev. E* **74**, 026405 (2006).
- [42] S. Dujko, R. D. White, Z. L. Petrović, R. E. Robson, and Z. L. Petrović, *Plasma Sources Science and Technology* **20**, 024013 (2011).
- [43] W. J. Goedheer and P. M. Meijer, *J. Nucl. Mater.* **200**, 282 (1993).
- [44] M. O. M. Mahmoud and M. Yousfi, *J. Appl. Phys.* **81**, 5935 (1997).
- [45] D. Loffhagen and R. Winkler, *J. Phys. D: Appl. Phys.* **34**, 1355 (2001).
- [46] R. D. White, R. E. Robson, B. Schmidt, and M. Morrison, *Journal of Physics D: Applied Physics* **36**, 3125 (2003).
- [47] S. Dujko, R. D. White, and Z. L. Petrović, *J. Phys. D: Appl. Phys.* **41**, 245205 (2008).
- [48] Z. L. Petrović, S. Marjanović, S. Dujko, A. Banković, G. Malović, S. Buckman, G. Garcia, R. White, and M. Brunger, *Applied radiation and isotopes* **83**, 148 (2013).
- [49] S. Dujko, Z. M. Raspopović, R. D. White, T. Makabe, and Z. L. Petrović, *The European Physical Journal D* **68**, 166 (2014).
- [50] R. D. White and R. E. Robson, *Phys. Rev. E* **84**, 031125 (2011).
- [51] R. D. White, R. E. Robson, B. Schmidt, and M. A. Morrison, *J. Phys. D: Appl. Phys.* **36**, 3125 (2002).
- [52] R. White and R. Robson, *Phys. Rev. Lett.* **102**, 230602 (2009).
- [53] J. G. Verwer and B. Sportisse, Technical Report MAS-R9830 **CWI** (1998).
- [54] K. A. Bagrinovskii and S. K. Godunov, *Dokl. Akad. Nauk SSSR (NS)* **115**, 431 (1957).
- [55] G. Strang, *SIAM J. Numer. Anal.* **5**, 506 (1968).
- [56] B. O. Dia and M. Schatzman, *Math. Mod. Numer. Anal.* **30**, 343 (1996).
- [57] T. Ohwada, *J. Comp. Phys.* **139**, 1 (1998).
- [58] A. Gerisch and R. Weiner, *Comp. Math. App.* **45**, 53 (2003).
- [59] L. Pareschi and G. Russo, *Adv. Theor. Comp. Math.* **3**, 269 (2000).

- [60] L. Pareschi and G. Russo, *SIAM. J. Numer. An.* **37**, 1217 (2005).
- [61] S. Gottlieb and C.-W. Shu, *Math. Comp.* **67**, 73 (1998).
- [62] J. Douglas, *Numer. Math.* **4**, 41 (1962).
- [63] J. Douglas and J. E. Gunn, *Numer. Math.* **6**, 428 (1964).
- [64] W. Hundsdorfer, *Applied Numerical Mathematics* **42**, 213 (2002).
- [65] A. D. Polyanin, *Handbook of Linear Partial Differential Equations for Engineers and Scientists*. (Chapman and Hall, Boca Raton, 2002).
- [66] M. Morales-Hernandez, P. Garcia-Navarro, and J. Murillo, *J. Comp. Phys.* **231**, 6532 (2012).
- [67] R. LeVeque, *Finite Difference Methods for Ordinary and Partial Differential Equations* (SIAM, Philadelphia, 2007).
- [68] J. P. Boris and D. L. Book, *J. Comp. Phys.* **11**, 38 (1973).
- [69] R. Courant, K. Friedrichs, and H. Lewy, *IBM J. Res. Dev.* **11**, 215 (1967).
- [70] A. Harten, *J. Comp. Phys.* **49**, 357 (1983).
- [71] S. Osher and S. Chakravarthy, *SIAM J. Numer. Anal.* **21**, 995 (1984).
- [72] P. L. Roe, Royal Aircraft Establishment Technical Report 81047 (1981).
- [73] S. T. Zalesak, *J. Comp. Phys.* **31**, 335 (1979).
- [74] P. K. Sweby, *SIAM J. Nume. Anal.* **21**, 995 (1984).
- [75] G. J. Boyle, M. J. E. Casey, R. D. White, Y. Cheng, and J. Mitroy, *J. Phys. D: Appl. Phys.* **47**, 345203 (2014).
- [76] G. J. Boyle, M. J. E. Casey, R. D. White, and J. Mitroy, *Phys. Rev. A* **89**, 022712 (2014).
- [77] G. J. Boyle, W. J. Tattersall, D. G. Cocks, S. Dujko, and R. D. White, *Phys. Rev. A* **91**, 052710 (2015).
- [78] R. Winkler, G. L. Braglia, A. Hess, and J. Wilhelm, *Beitr. Plasmaphys.* **24**, 657 (1984).
- [79] D. Loffhagen and R. Winkler, *J. Phys. D: Appl. Phys.* **29**, 618 (1996).
- [80] H. Leyh, D. Loffhagen, and R. Winkler, *Comp. Phys. Comm.* **113**, 33 (1998).
- [81] L. Huxley and R. Crompton, *The Diffusion and Drift of Electrons in Gases* (Wiley, New York, 1974).
- [82] S. Dujko, Z. M. Raspopovic, and Z. L. Petrovic, *J. Phys. D: Appl. Phys.* **38**, 2952 (2005).
- [83] W. J. Tattersall, D. G. Cocks, G. J. Boyle, S. J. Buckman, and R. D. White, *Phys. Rev. E* **91**, 043304 (2015).
- [84] M. Wertheim, *Phys. Rev. Lett.* **10**, 321 (1963).

- [85] E. Thiele, *J. Chem. Phys.* **39**, 474 (1963).
- [86] L. Verlet and J. Weis, *Phys. Rev. A* **5**, 939 (1971).
- [87] W. Meegen and P. Pusey, *Phys. Rev. A* **43**, 5429 (1991).
- [88] G. J. Boyle, R. D. White, R. E. Robson, S. Dujko, and Z. L. Petrovic, *New J. Phys.* **14**, 045011 (2012).
- [89] J. Fletcher, *J. Phys. D: Appl. Phys.* **18**, 221 (1985).
- [90] P. Segur, A. Alkaa, S. Pineau, Z. A. A. Chouki, C. Moutarde, and S. Laffront, *Plasma Sources Sci. Technol.* **4**, 183 (1995).
- [91] G. Petrov and R. Winkler, *J. Phys. D: Appl. Phys.* **30**, 53 (1997).
- [92] R. D. White, R. E. Robson, P. Nicoletopoulos, and S. Dujko, *The European Physical Journal D* **66**, 117 (2012).
- [93] M. Foxe, C. Hagmann, I. Jovanovic, A. Bernstein, K. Kazkaz, V. Mozin, S. V. Pereverzev, S. Sangiorgio, and P. Sorensen, *Nucl. Instr. Meth. Phys. Res. A* **771**, 88 (2015).
- [94] S. Chen, R. P. McEachran, and A. D. Stauffer, *J. Phys. B* **41**, 025201 (2008).
- [95] J. Yarnell, M. Katz, R. Wenzel, and S. Koenig, *Phys. Rev. A* **7**, 2130 (1973).